

Cavity-QED Simulation of a Maser beyond the Mean-Field Approximation

Xinpeng Shu*, Yining Jiang†, Hao Wu and Mark Oxborrow

Department of Materials, Imperial College London, Exhibition Road, South Kensington, SW7 6AZ, UK.

ABSTRACT

We here introduce a method for simulating, quantum mechanically, the dynamics of a maser where the strength of the magnetic field of the microwave mode being amplified by stimulated emission varies over the volume of the maser’s spatially extended gain medium. This is very often the case in real systems. Our method generalizes the well-known Tavis-Cummings (T-C) model of cavity quantum electrodynamics (QED) to encompass quantum emitters whose coupling strengths to the maser’s amplified mode vary over a distribution that can be accurately determined using an electromagnetic-field solver applied to the maser cavity’s geometry and composition. We then solve our generalized T-C model to second order in cumulant expansion using publicly available Python-based software. We apply our methodology to a specific, experimentally measured maser based on an optically pumped crystal of pentacene-doped *para*-terphenyl. We demonstrate that certain distinct quantum-mechanical features exhibited by this maser’s dynamics, most notably the observation of Rabi-like flopping associated with the generation of spin-photon Dicke states, can be accurately reproduced using our numerically solved model. The equivalent simpler model, that invokes the mean-field approximation, fails to do so. By constructing then solving for artificial (perfectly Gaussian) distributions, we go on to explore how the performance of this type of maser is affected by the spread in spin-photon coupling strengths. Our methodology thereby enables the maser’s anatomy to be more rationally engineered.

I. INTRODUCTION.

Largely out of necessity, simulations of quantum-mechanical systems very often incorporate a cascade of rather drastic approximations, many of which are uncontrolled. Their names include (this list is far from exhaustive and in no particular order): adiabatic, Born, rotating-wave [1], Markovian, weak-coupling, impulse, finite-dimensional, Trotter, and mean-field. This paper quantitatively assesses the validity of the last of these, as it has been applied over recent years to the simulation of optically-pumped masers.

As the expansion of the well-chosen acronym might suggest, a “maser”, the microwave equivalent of a laser, works through the stimulated emission of electromagnetic radiation from atoms (or an equivalent form of emitter) [2]. Such radiation is coherent (with its stimulus). Very often, to boost the rate of such emission, the atoms are placed inside some form electromagnetic (“build-up”) cavity, that resonates in a particular “mode” at a particular frequency. Excitement over this venerable class of device has been rekindled in recent years by the fact that optically-pumped solid-state masers, based on

emissively spin-polarized materials, provide experimental access to the strong-coupling regime of cavity quantum electrodynamics (cavity-QED), using convenient bench-top set-ups in open air at room temperature (RT) [3, 4]. Such a maser harnesses a population inversion between two paramagnetic sub-levels, such as X and Z in the case of the triplet ground state of molecular pentacene, where this inversion is generated by some or other pumping mechanism (namely, spin-selective intersystem crossing, ISC, in the case of pentacene). This X - Z transition exhibits features including: (a) dipolar coupling between two unpaired electrons, described by zero-field splitting (ZFS) [5, 6]; (b) considerable population inversion; (c) substantial lifetime of sublevel Z at room temperature [5]; (d) slow spin-lattice relaxation ($>330 \mu\text{s}$ [7]) even at high operating temperature.

Due to its fame and utility in applications spanning (i) single-spin optically detected magnetic resonance (ODMR) [8], (ii) dynamic nuclear polarization (DNP) [9], and (iii) optically-pumped solid-state masing at RT, the spin dynamics of pentacene-doped *para*-terphenyl crystal (henceforth “Pc:PTP”) [2] has been extensively studied [10]-[12].

*contact author: xinpeng.shu23@imperial.ac.uk

† contact author: yining.jiang23@imperial.ac.uk

In a solid-state maser, it is generally advantageous for the number of atoms/molecules, N , interacting with the microwave mode being amplified to be as large as possible, and for these atoms to be emissively polarized. In other words, a (pumped) material exhibiting high spin-polarization density, where this material substantially fills the mode, is advantageous. In typical experiments, N ranges from 10^{16} to 10^{19} [9,10,13,14,15]. These conditions allow for the generation of a high co-operativity [13, 16], so exceeding the threshold for masing (either amplification or oscillation) and/or for Dicke’s super-radiance [14,15].

With regard to simulating of these systems using a computer, the very large number of atoms involved poses an immediate difficulty: formally, the operators (including the Hamiltonian) required to represent the system quantum mechanically are $2^N \times 2^N$ matrices. The well-known Mean-Field Approximation (MFA), was applied by Pierre-Ernest Weiss in the early 20th century to explain ferromagnetism. It provides an elegant way to simplify many-body problems by replacing the innumerable combinations of states of individual, nominally identical particles with an averaged “mean” state or field. The MFA has found extensive applications in various areas of quantum simulation [14,15] towards reducing the size (in particular in terms of computer memory) of the representation required. The MFA allows for the simulation of large numbers of atoms/molecules by treating them as a single, collective “super” atom, neglecting any higher (internal) correlations between the individual atoms that compose this super atom.

While it significantly reduces the computational burden, the MFA dismisses the fact that, in reality, the atoms within a maser *do* differ from one another: Firstly, a applied D.C. magnetic field might not be spatially uniform, meaning that the maser transition frequency of one atom will differ from that of another atom (by way of Zeeman effect) located at a different point in space; this effect gives rise to the so-called “field broadening” of peaks in NMR or EPR spectroscopy. Secondly, and more germane to the work we present here, the coupling between an atom’s maser transition (between two paramagnetic levels) and the A.C. magnetic field associated with the maser’s operational electro-magnetic mode will also vary depending on where the atom is located in space. This variance occurs since the amplitude and/or orientation of the mode’s A.C. magnetic field (very often a type of “standing wave”) will not be spatially

*contact author: xinpeng.shu23@imperial.ac.uk

† contact author: yining.jiang23@imperial.ac.uk

uniform. Either type of magnetic-field gradient (D.C. or A.C.) will impact on the maser’s performance (or that of the same material used for DNP, ODMR or magnetometry).

To date, most quantum-mechanical models developed for simulating masers in the strong coupling regime, leading to the observation of so-called “Dicke states” [4, 6], have taken the Mean-Field Approximation, so eliminating the effects of magnetic field gradients by design. In contrast, our study here goes beyond the MFA: it accurately quantifies how variation in the atom-field coupling across an ensemble of non-identical atoms affects maser performance. It thereby provides an implementable methodology for more realistically simulating experimental devices.

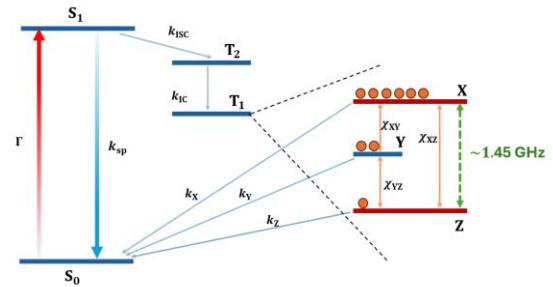


FIG 1 A Jablonski diagram showing the mechanism of pentacene as the gain medium of a maser. The three energy levels X, Y, and Z on the right are the sublevels of the triplet T₁. The maser transition with a frequency of 1.4495 GHz occurs between X and Z (green and dashed line). Γ is the pumping rate; k_{sp} is the spontaneous emission rate; k_{isc} is the intersystem crossing (ISC) rate; k_{ic} is the internal conversion rate; χ_{xz} , is the spin-lattice relaxation rate between sublevels X and Z, similarly for χ_{xy} , χ_{yz} . k_x , is the decay rate from sublevel X, to the ground state S₀, similar for k_y and k_z

II. MECHANISM OF MASER OPERATION

How pentacene-doped *para*-terphenyl (Pc: Ptp) serves as the gain medium of a maser is shown in Figure 1. Pentacene molecules in the ground state S₀ are optically pumped to the first singlet state S₁ after absorbing photons with wavelengths shorter than 590 nm [5]. The rate of the optical-pump process from S₀ to S₁ can be calculated as $\Gamma = \eta_{opt} P_{pump} / h f_{pump}$ [6]. P_{pump} and f_{pump} represent the instantaneous power and frequency of the light source used to excite the pentacene molecules, respectively. h is Planck’s constant. η_{opt} is a dimensionless factor that accounts for the energy losses during the optical-pump process

of pentacene molecules. The process of pentacene molecules returning from S_1 to S_0 is mainly dominated by spontaneous emission [6]. The other pentacene molecules in S_1 first transfer to the second triplet state T_2 through intersystem crossing (ISC) with spin-orbit coupling, then rapidly relax to the first triplet state T_1 through internal conversion (IC) [7]. The ISC process is highly spin-selective, resulting in a population ratio of 0.76 : 0.16 : 0.08 [10] among the sublevels T_X , T_Y and T_Z in T_2 . The IC process preserves this ratio in T_1 's sublevels X, Y, and Z [7]. When the energy of the photon (with a microwave frequency of around 1.45 GHz) matches the energy gap between X and Z in the maser cavity, stimulated emission occurs, harvesting the population inversion between X and Z. During the stimulated emission process, the population inversion is affected both by spin-lattice relaxation between different sublevels and by non-radiative decay from the triplet to S_0 . Masing occurs when the number of photons generated by stimulated emission exceeds the number of photons lost either through dissipation (Joule heating in metal surfaces, dielectric losses) within the maser cavity itself or else through extraction from the cavity by a coupling loop.

III. MASER ASSEMBLY AND OPERATION

The experimental embodiment of the optically pumped Pc:Ptp maser that we simulate here is described in the previous work by Wu *et al.* [6]. As shown in figure 2 (a), the gain medium comprises a *para*-terphenyl single crystal, where 0.1% of its molecules have been replaced randomly by pentacene as a solid solution. The crystal is placed in the bore of a strontium titanate (STO) dielectric ring that serves as a “flux concentrator” for the magnetic field of the copper cavity’s TE_{018} mode. This arrangement helps to boost the strength of coupling between the mode and the X-Z transitions of the pentacene molecules (in their photo-excited triplet ground states) resident inside the bore. The ring has an inner diameter of 4.05 mm, an outer diameter of 12 mm and a height of 8.6 mm. The STO ring is held 3 mm above a copper deck plate by a support made of cross-linked polystyrene (“Rexolite”) and placed inside a copper enclosure.

The relative dielectric constant of STO is taken to be $\epsilon_r \approx 316$ [17] (dielectrically, the material is isotropic).

The maser is pumped by single pulses from a cerium-doped yttrium-aluminum-garnet (YAG) luminescent

concentrator (Ce: YAG LC) [6], itself pumped by a xenon flash lamp, experimentally achieving continuous masing up to 4 ms in duration.

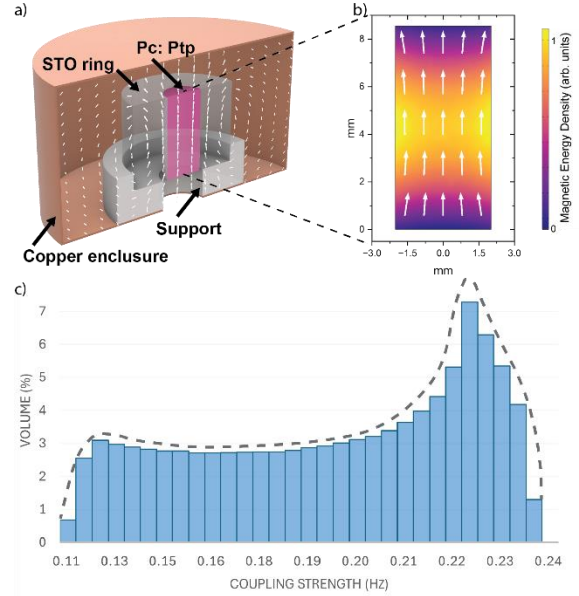


FIG 2 (a) Rendered image of the maser cavity. The magnetic vector field (white arrows) is provided by a COMSOL simulation. (b) The magnetic energy density map and magnetic field vector on a plane cut through the middle of gain medium. (c) distribution of coupling strength through the bore of STO dielectric ring [as shown in (b)].

COMSOL’s “RF Module”, incorporating a 2.5 D axisymmetric model of the maser’s electromagnetic cavity, is used to obtain the magnetic energy density and magnetic field vector, and thereupon provide the distribution of coupling strengths throughout the volume occupied by the maser crystal inside the maser cavity. In COMSOL, each electromagnetic mode obeys the standard Maxwellian wave equation (for the electric field): $\nabla \times \mu_r^{-1}(\nabla \times \mathbf{E}) - k_0^2 \epsilon_r \mathbf{E} = \mathbf{0}$. An impedance boundary condition is applied to the cavity’s internal metal walls: $\sqrt{\frac{\mu_0 \mu_r}{\epsilon_0 \epsilon_r - j \frac{\sigma}{\omega}}} \mathbf{n} \times \mathbf{H} - (\mathbf{n} \cdot \mathbf{E}) \mathbf{n} = (\mathbf{n} \cdot \mathbf{E}_s) \mathbf{n} - \mathbf{E}_s$, where the first term on the left-hand side describes the material’s surface impedance and the right hand-side incorporates the surface electric field \mathbf{E}_s . Our simulation yields electric and magnetic field profiles of the cavity’s TE_{018} mode. Keeping the as-measured geometry of the cavity (as drawn in COMSOL) fixed, the dielectric

*contact author: xinpeng.shu23@imperial.ac.uk

† contact author: yining.jiang23@imperial.ac.uk

constant of STO was adjusted by a few percent to such that the frequency of our simulated TE_{018} mode exactly matched the frequency of Pc:Ptp's X - Z transition (at room temperature), namely 1.4495 Hz (to 5 sig. fig.), as observed experimentally [3,6,10].

Figures 2 (a) and (b) show how the TE_{018} mode's A.C. magnetic field (white arrows) is "funneled" through the bore of the STO ring. For simplicity, the effect of the slight tilt in the magnetic field away from axial is not included in our simulation. The spatial variation of the spin-photon coupling strength, represented by the yellow-purple false-color plot in fig. 2 (b) is calculated as: $g_s = \gamma \sqrt{\mu_0 \hbar f_{mode} / 2V_{mode}^i}$, where γ is the electron gyromagnetic ratio, μ_0 is the permeability of free space, \hbar is Planck's constant, f_{mode} is the cavity's (*i.e.*, the TE_{018} mode's) resonance frequency and V_{mode}^i is the effective magnetic mode volume for the i -th molecule, expressed as the ratio of the stored magnetic energy within the cavity, to the magnetic field energy density at the location of the i -th molecule:

$$V_{mode}^i = \frac{\frac{1}{2} \int \mu_0 |\mathbf{H}(\mathbf{r})|^2 dV}{\frac{1}{2} \mu_0 |\mathbf{H}_i(\mathbf{r})|^2} \quad (1)$$

IV. QUANTUM MASTER EQUATIONS BEYOND MEAN-FIELD APPROXIMATION

Directly simulating the 3.32×10^{17} pentacene molecules within our maser cavity would require huge matrices and astronomical computer resources. Instead, we divide these molecules into M "clusters", where M is a reasonably small, finite integer (for the simulations below, we take $M = 31$). Anatomically, each cluster corresponds to the volume or "shell" of gain material that lies between two surfaces of constant magnetic field strength, the strength differing by a small finite amount (a "step") between the two surfaces. We assume the pentacene molecules belonging to the same cluster are exposed to the same strength of A.C. magnetic field. The j -th cluster contains N_j nominally identical pentacene molecules; for a uniformly doped gain medium, this number is proportional to the volume of crystal (in the shape of the above-mentioned "shell") apportioned to the cluster. Every pentacene molecule in the j -th cluster couples to the electromagnetic field with the same coupling strength g_j , as shown in figure 2. Based on the above assumptions, we describe the system's

dynamics by an extended Tavis-Cummings-like Hamiltonian, in the rotating frame of the spins after applying the rotating-wave approximation:

$$\hat{H} = \Delta \hat{a}^\dagger \hat{a} + \sum_{j=1}^M \sum_{i=1}^{N_j} g_j (\hat{a}^\dagger \hat{\sigma}_i^{\text{ZX}} + \hat{a} \hat{\sigma}_i^{\text{XZ}}). \quad (2)$$

Here, $\Delta = \omega_c - \omega_{\text{XZ}}$, ω_c is the angular velocity of the electromagnetic field in the cavity, and ω_{XZ} is the angular velocity of the spin transition between $|X\rangle$ and $|Y\rangle$. For any two states α and β , $\hat{\sigma}_i^{\beta\alpha} = (\hat{\sigma}_i^{\alpha\beta})^\dagger = |\beta\rangle_i \langle \alpha|_i$ represents the operator of the spin transition for the i -th molecule from α to β . \hat{a}^\dagger (\hat{a}) is the creation (annihilation) operator that generates (destroys) a photon in the cavity. Transitions between the energy levels of the pentacene molecules shown in Figure 1, and the dissipation of photons within the cavity, are generated by the following Liouvillians:

$$\begin{aligned} \mathcal{L}_{Pmp}[\hat{\rho}] &= \sum_{j=1}^M \sum_{i=1}^{N_j} \left(\sum_l P_l \Gamma \eta_{\text{ISC}} \mathcal{D}[\hat{\sigma}_i^{\text{LS}_0}] \hat{\rho} \right) \\ \mathcal{L}_{\text{RLX}}[\hat{\rho}] &= \sum_{j=1}^M \sum_{i=1}^{N_j} \left(\sum_{l,m;l \neq m} \chi_{lm} \mathcal{D}[\hat{\sigma}_i^{lm}] \hat{\rho} \right) \\ \mathcal{L}_{\text{DCY}}[\hat{\rho}] &= \sum_{j=1}^M \sum_{i=1}^{N_j} \left(\sum_l k_l \mathcal{D}[\hat{\sigma}_i^{\text{S}_0 l}] \hat{\rho} \right) \\ \mathcal{L}_{\text{PH}}[\hat{\rho}] &= k_C (1 + n_{\text{mth}}) \mathcal{D}[a] \hat{\rho} + k_C n_{\text{mth}} \mathcal{D}[\hat{a}^\dagger] \hat{\rho} \end{aligned} \quad (3)$$

Sublevels of the triplet state are represented here by l and m ($l, m \in \{X, Y, Z\}$, $l \neq m$). $\mathcal{D}[\hat{\rho}] \hat{\rho} = 2\hat{\rho} \hat{\rho}^\dagger - \hat{\rho}^\dagger \hat{\rho} \hat{\rho} - \hat{\rho} \hat{\rho}^\dagger \hat{\rho}$ is the Lindblad operator for any operator $\hat{\rho}$. Due to the high rate of IC from T_2 to T_1 , we use $\mathcal{L}_{Pmp}[\hat{\rho}]$ to generate transitions of pentacene molecules from S_0 via S_1 then T_2 directly into the sublevels of T_1 . The values of P_X , P_Y , and P_Z are 0.76, 0.16 and 0.08, respectively, which corresponds to the initial population distribution among the X, Y and Z sublevels as generated by the spin-selective ISC process [10]. η_{ISC} is the overall ISC yield, calculated as $\eta_{\text{ISC}} = k_{\text{ISC}} / (k_{\text{ISC}} + k_{\text{SP}})$. The rate of pumping pentacene molecules from S_0 to any sublevel l of T_1 can be given by $P_l \Gamma \eta_{\text{ISC}}$. $\mathcal{L}_{\text{RLX}}[\hat{\rho}]$ represents the spin-lattice relaxation between the three sublevels of T_1 . $\mathcal{L}_{\text{DCY}}[\hat{\rho}]$ describes the nonradiative decay from different sublevels back to S_0 . $\mathcal{L}_{\text{PH}}[\hat{\rho}]$ represent the thermal dissipation of photons within the cavity. At zero kelvin, photons are lost from the cavity at the rate of k_C (per photon); n_{mth} is the number of thermal photons in the cavity that can be calculated as $n_{\text{mth}} =$

*contact author: xinpeng.shu23@imperial.ac.uk

† contact author: yining.jiang23@imperial.ac.uk

$1/(\exp[\hbar\omega_c/(k_B T)] - 1)$, where k_B is the Boltzmann constant and T is the temperature. Alongside the processes mentioned above, we also include a Liouvillian to describe the spin-dephasing process of the pentacene triplets: $\mathcal{L}_{dphs}[\hat{\rho}] = \sum_{j=1}^M \sum_{i=1}^{N_j} (\sum_l k_S \mathcal{D}[\hat{\sigma}_i^l]) \hat{\rho}$, where k_S is the spin-dephasing rate and $\hat{\sigma}_i^l$ represents the projection operators for the i -th pentacene molecule in the l -th sublevel.

The time derivative of the expectation value of any operator \hat{O} can be calculated from [11]:

$$\begin{aligned} \frac{d}{dt} \langle \hat{O} \rangle &= \text{tr} \left(\hat{O} \frac{d}{dt} \langle \hat{\rho} \rangle \right) \\ \frac{d}{dt} \langle \hat{\rho} \rangle &= -i[\hat{H}, \hat{\rho}] + \sum \mathcal{L}[\hat{\rho}]. \end{aligned} \quad (4)$$

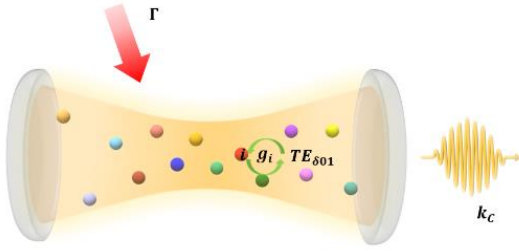


FIG 3. Schematic illustration of the quantum model. The “mirrors” on the left- and right-hand sides represent the boundaries of the (microwave) cavity. The orange area represents the magnetic field of the $TE_{01\delta}$ mode in the cavity with a frequency of $\omega_c/2\pi$. The differently colored spheres represent clusters composed of a certain number of identical pentacene molecules. The coupling strength between the i -th cluster and the magnetic field is g_i . The red arrow indicates the external optical pump with a rate of Γ . The yellow wavelet on the right represents photons escaping from the cavity at a rate of κ_c .

To solve the dynamics of the photon number in the cavity, we need a set of closed differential equations. Here we use the quantum cumulant expansion [12] up to the second order. The final equations that we obtain are:

$$\begin{aligned} \frac{d}{dt} \langle \hat{a}^\dagger \hat{a} \rangle &= k_c n_c^{th} - k_c \langle \hat{a}^\dagger \hat{a} \rangle + \text{Im} \sum_j^M N_j g_j \langle \hat{a} \hat{\sigma}_j^{XZ} \rangle \\ &\quad - \text{Im} \sum_j^M N_j g_j \langle \hat{a}^\dagger \hat{\sigma}_j^{ZX} \rangle \end{aligned} \quad (5)$$

$$\begin{aligned} \frac{d}{dt} \langle \hat{N}_{x,j} \rangle &= P_x \Gamma \eta_{ISC} - \chi_{XZ} (\langle \hat{N}_{x,j} \rangle - \langle \hat{N}_{z,j} \rangle) - k_x \langle \hat{N}_{x,j} \rangle \\ &\quad - \chi_{XY} (\langle \hat{N}_{x,j} \rangle - \langle \hat{N}_{y,j} \rangle) - \text{Im} N_j g_j \langle \hat{a} \hat{\sigma}_j^{XZ} \rangle \\ &\quad + \text{Im} N_j g_j \langle \hat{a}^\dagger \hat{\sigma}_j^{ZX} \rangle \end{aligned} \quad (6)$$

$$\begin{aligned} \frac{d}{dt} \langle \hat{N}_{y,j} \rangle &= P_y \Gamma \eta_{ISC} - \chi_{YX} (\langle \hat{N}_{y,j} \rangle - \langle \hat{N}_{x,j} \rangle) - k_y \langle \hat{N}_{y,j} \rangle \\ &\quad - \chi_{YZ} (\langle \hat{N}_{y,j} \rangle - \langle \hat{N}_{z,j} \rangle) \end{aligned} \quad (7)$$

$$\begin{aligned} \frac{d}{dt} \langle \hat{N}_{z,j} \rangle &= P_z \Gamma \eta_{ISC} - \chi_{ZX} (\langle \hat{N}_{z,j} \rangle - \langle \hat{N}_{x,j} \rangle) - k_z \langle \hat{N}_{z,j} \rangle \\ &\quad - \chi_{ZY} (\langle \hat{N}_{z,j} \rangle - \langle \hat{N}_{y,j} \rangle) + \text{Im} N_j g_j \langle \hat{a} \hat{\sigma}_j^{XZ} \rangle \\ &\quad - \text{Im} N_j g_j \langle \hat{a}^\dagger \hat{\sigma}_j^{ZX} \rangle \end{aligned} \quad (8)$$

$$\begin{aligned} \frac{d}{dt} \langle \hat{a} \hat{\sigma}_j^{XZ} \rangle &= -\frac{k_x + k_z + \chi_{xy} + \chi_{yz} + k_s + k_c}{2} \langle \hat{a} \hat{\sigma}_j^{XZ} \rangle \\ &\quad - i g_j (N_j - 1) (\langle \hat{\sigma}_j^{XZ} \hat{\sigma}_j^{ZX} \rangle) - \sum_{k, j \neq k}^M N_k g_k \langle \hat{\sigma}_j^{XZ} \hat{\sigma}_k^{ZX} \rangle \\ &\quad - i g_j \left(\frac{\langle \hat{N}_{x,j} \rangle}{N_j} \right) - \frac{\text{Im} g_j \langle \hat{a}^\dagger \hat{a} \rangle (\langle \hat{N}_{x,j} \rangle - \langle \hat{N}_{z,j} \rangle)}{N_j} \end{aligned} \quad (9)$$

$$\begin{aligned} \frac{d}{dt} \langle \hat{\sigma}_j^{XZ} \hat{\sigma}_k^{ZX} \rangle &= -(k_x + k_z + \chi_{xy} + \chi_{yz} + k_s) \langle \hat{\sigma}_j^{XZ} \hat{\sigma}_k^{ZX} \rangle \\ &\quad - \frac{\text{Im} g_j \langle \hat{a}^\dagger \hat{\sigma}_k^{ZX} \rangle (\langle \hat{N}_{x,j} \rangle - \langle \hat{N}_{z,j} \rangle)}{N_j} \\ &\quad + \frac{\text{Im} g_k \langle \hat{a} \hat{\sigma}_j^{XZ} \rangle (\langle \hat{N}_{x,k} \rangle - \langle \hat{N}_{z,k} \rangle)}{N_k} \end{aligned} \quad (10)$$

Here, we use $\langle \hat{\sigma}_j^{\beta\alpha} \rangle$ to replace all $\langle \hat{\sigma}_i^{\beta\alpha} \rangle$ (for i from 1 to N_j) in the j -th cluster since we assume that all pentacene molecules in the j -th cluster are identical. $\langle \hat{N}_{x,j} \rangle = N_j \langle \hat{\sigma}_j^{ll} \rangle$ represents the expectation value of the population on the l sublevel. “Im” represents the imaginary part.

V. COMPARISON BETWEEN SIMULATIONS AND EXPERIMENTAL RESULTS

In the experiment, we set a single pulse from the xenon lamp to last 3 ms with a fluence of 2.07 J/cm^2 . The pumping curve (*i.e.*, the time profile of the intensity of the optical pumping) is recorded by a pyroelectric

*contact author: xinpeng.shu23@imperial.ac.uk

† contact author: yining.jiang23@imperial.ac.uk

sensor (Thorlabs ES245C), and displayed in the upper panel of Figure 4.

The optical pumping area is approximately 1.7 cm^2 [6]. According to a similar experiment [18], about 17 % of the power is transferred to Pc:Ptp. Here we estimate that the instantaneous pump power for pentacene molecules is approximately 150 W. The raw pumping curve displays a sharp peak when the xenon flash lamp is first ignited (the optical pumping intensity during this spike is a few times greater than what it is subsequently). This peak may result from the rapid increase of energy when the pulse is activated, driving the pyroelectric sensor beyond equilibrium. It would appear similar to the overshoot phenomena reported for pyroelectric sensors under faster ephemeral rates and/or insufficient settle-down time [19, 21]. This artefact is removed from the fitted pumping curve used in our simulation –see the upper panel in Figure 4. For simplicity (no attempt at accurately modeling the switch-off dynamics was made), the intensity of the pump is set to zero at 3 ms onwards post ignition; again see Figure 4. The maser’s oscillatory output at 1.4495 GHz is detected by a logarithmic detector (Analog Devices AD8318) and recorded using a digital storage oscilloscope (Tektronix TBS 1102B-EDU, 2-gigasamples/s sampling rate, 100-MHz bandwidth) –see the red curve in the lower panel of Figure 4.

In this section of our paper, we conduct two different simulations: Our first simulation is based on the distribution of coupling strengths that correspond to the experimental set described above and Ref [6]. We divide the 3.32×10^{17} pentacene molecules into 31 “clusters” ($M = 31$). The number of pentacene molecules (N_j) and the coupling strength (g_j) assigned to the j -th cluster are determined by the distribution of coupling strengths within the Pc:Ptp crystal (see Figure 2) -as calculated using COMSOL. In our second simulation, we invoke the mean-field approximation (MFA), corresponding to $M = 1$; this provides a baseline for comparison. The MFA has been widely applied to the simulation of masers based on NV centers and pentacene molecules [6, 16, 21]. Only one universal cluster is used, set at a coupling strength of $g_s = \gamma \sqrt{\mu_0 h f_{mode} / 2V_{mode}} = 0.23 \text{ Hz}$ for all pentacene molecules, irrespective of their location and the amplitude of A.C. magnetic field to which they are exposed. Here, V_{mode} is the magnetic mode volume in of TE_{018} mode inside the cavity. We find that our simulation fits the experimental data best

*contact author: xinpeng.shu23@imperial.ac.uk

† contact author: yining.jiang23@imperial.ac.uk

when our optical-coupling-efficiency parameter η_{opt} is set to 6.12 %. We suspect that the smallness of this parameter reflects inhomogeneous broadening, where a large fraction of the pumped (and thus spin-polarized) pentacene molecules are detuned so far from the TE_{018} mode’s frequency that they cannot contribute to masing. The value of $\langle \hat{a}^\dagger \hat{a} \rangle$ as a function of time is found by solving (*i.e.* integrating up w.r.t. time) equations (4)-(9). We calculate the maser’s output power P_{maser} from $\langle \hat{a}^\dagger \hat{a} \rangle$ by the expression $P_{\text{maser}} = h f_{mode} \langle \hat{a}^\dagger \hat{a} \rangle k_c k / (1 + k)$ [4]. k is the coupling coefficient of the output of the cavity, here we set it as 1. The other required parameters are provided in this paper’s appendix.

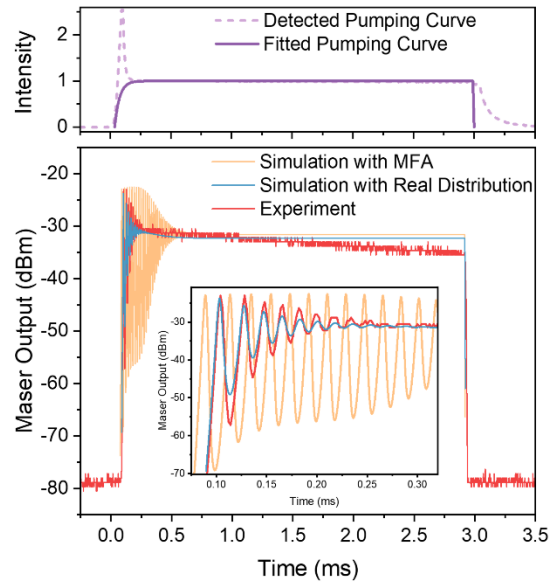


FIG 4. Upper panel: The detected pumping curve (light purple and dashed line) and fitted pumping curve (purple) after normalizing the intensity such that, in arbitrary units, its value along the curve’s plateau (from 0.25 to 3 ms) equals unity. Lower panel: microwave power output as a function of time: the experimentally measured curve (red), the simulated curve for a realistic distribution of couplings (blue-gray), and the simulated results under the MFA (orange); all for the optical pump pulse shown in the upper panel. The inset shows an enlargement of the Rabi oscillations that occur at the beginning of the maser burst.

In the experimental results (see figure 4), we observe a period of Rabi (-like) oscillations at the beginning of the maser burst after the optical pump is turned on. The maximum microwave power extracted is around -24 dBm and the oscillations last for approximately 0.25 ms. These oscillations are caused by the coupling of

microwave photons with the spin transitions between X and Z so forming a hybrid Dicke (-like) state.

Our simulation using a realistic distribution of coupling strengths convincingly reproduces the frequency and duration of the experimental observed Rabi oscillations. We note, however, that the amplitude of oscillations in the simulation is slightly smaller than that in the experimental results. This discrepancy could be because our simulation assumed a uniform pumping rate for each molecule without considering the spatial variation in optical intensity (thus pumping rate) across the Pc:Ptp crystal. For our $M = 1$ simulation invoking the MFA, the oscillations do not fit at all well with the experimental results and show a much longer duration of nearly 0.75 ms. We speculate that this is because the coupling strength calculated directly using the expression $g_s = \gamma \sqrt{\mu_0 \hbar f_{mode} / 2V_{mode}}$ is greater than the average value in the distribution of coupling strengths.

After the Rabi oscillations have petered out, the outputted microwave power remains broadly constant. The slight negative slope observed experimentally (red curve) was already reported in a study using the MFA to simulate maser experiments [6]. We suspect it is a symptom of thermal loading (and thus heating up) of the Pc:Ptp crystal and/or its surrounding STO ring. The envisaged effects of such heating include both (i) a monotonically increasing detuning $\Delta = \omega_c - \omega_{XZ}$ between the frequency of the cavity's TE_{018} mode and that of pentacene's X-Z transition [20] and (ii) changes in the values of rate constants that define the pentacene's spin dynamics; the rates of spin-lattice relaxation should certainly decrease with temperature [16]. None of these thermal affects are included in our simulations.

VI. COUPLING STRENGTH UNDER GAUSSIAN NORMAL DISTRIBUTION

Instead of fitting our extended “ M -clusters” model to experimental data, we here use it to perform an array of thought (“*gedanken*”) experiments/simulations towards better understanding the extent to which a variation in coupling strength affects maser performance. Here the distribution of coupling strength is Gaussian but of varying width (*i.e.*, of varying standard deviation).

The number of clusters used remains fixed at $M = 31$; this is a manageable number given the modest

*contact author: xinpeng.shu23@imperial.ac.uk

† contact author: yining.jiang23@imperial.ac.uk

computational resources used. All extended simulations reported here were performed on a lab-top, each taking a few minutes to run. The *average* value of coupling strength is controlled to be the same as that used for our mean-field approximation, namely $g_s = 0.23$ Hz. The fraction of molecule belonging to each cluster follows a Gaussian normal distribution with a width (standard deviation) of σ Hz. Simulations were run for five different values of σ , namely 0 (corresponding to the MFA), 0.023, 0.046, 0.069, and 0.092.

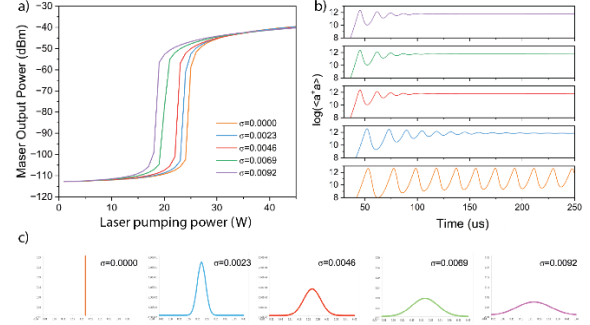


FIG 5 (a) continuous (CW) maser output power versus threshold applied optical pump (laser) power, indicating the threshold for maser oscillation, for 5 different widths σ in the distribution of coupling strengths; b) dynamics of the cavity photon number for a pentacene maser whose spin-photon coupling strength varies over a Gaussian normal distribution with standard deviations of 0, 0.0023, 0.0046, 0.0069, 0.0092, respectively. (c) These five different Gaussian normal distributions are here shown.

With an increased standard deviation, the pumping threshold decreases, the Rabi frequency increases, and the initial delay between the start of optical pumping and the onset of masing is shortened. A principal figure of merit for a maser is its cooperativity, $C = 4g_s^2 N / \kappa_c \kappa_s$, where $\kappa_c = \omega_c / Q$ is the cavity mode decay rate, and Q is the cavity's quality factor (for the TE_{018} mode) and $\kappa_s = 2 / T_2^*$ is the spin dephasing rate. The threshold condition for maser oscillation is simply $C > 1$. Here, the magnetic Purcell factor is key to enhancing maser performance and contributing to the factor of g_s^2 / κ_c in the cooperativity. And the optical power threshold is inversely proportional to the magnetic Purcell factor, $P_{optical} \propto g_s^2 / \kappa_c \propto V_m / Q$, the equation of which can be derived from the steady-state conditions of a two-level system [22]:

$$P_{optical} = \frac{\hbar^2 c_0 \chi_{XZ} (k_X + k_Z) + k_X k_Z}{\lambda \kappa \eta P_X k_Z - P_Z k_X} \times \frac{1}{C}$$

where λ is the optical pump wavelength, κ is the optical coupling efficiency, η is the intersystem crossing yield, χ_{XZ} is the spin-lattice relaxation rate between the $|X\rangle$ and $|Z\rangle$ sublevels, P_X and P_Z are the population ratios of the $|X\rangle$ and $|Z\rangle$, and k_X and k_Z are their decay rates back to ground state. Above parameters forms the left part of “ \times ” are data measured experimentally, while the cooperativity on the right side reflects the properties of microwave cavity, which is the main concern of this simulation, that determines the pumping threshold.

The Rabi frequency, $\Omega_{Rabi} = -\gamma_e C \sqrt{P_{MW}} / \sqrt{2}$, is strongly related to the cooperativity as well. It displays an increase with larger standard distribution σ . The time delay between the onset of optical pumping and the first peak of Rabi oscillation, which is believed to be affected by both the finite number of pentacene molecules in the gain medium and the Q factor, is also reduced with an increase in the spread of coupling strengths. With the average of the coupling strength controlled to be the same as the mean-field baseline simulation, the above favorable features brought about by a distribution of coupling strengths might be attributed to those particular clusters of stronger-than-average coupling strength: As a the standard deviation σ increases, a larger proportion of atoms have higher coupling strength (though a larger fraction also has lower). Furthermore, the collective behavior between clusters indicates that, although the spin-cavity interaction is still technically in the weak-coupling regime, synergistic effects (reminiscent of strong coupling) are still evident. The strict condition of achieving strong coupling is $2g > [\kappa + \gamma]/2$ [23], indicating that the coupling strength should be sufficiently large to overcome the energy dissipation process and thereby exhibit coherent Rabi oscillations. In our system on the other hand, exhibiting shorter-lived Rabi-like oscillations with increased standard deviation in coupling strength, suggests a partial transition towards strong coupling, leading to a collective coupling strength of an ensemble of N molecules with cavity $g_e \gg (\kappa, \gamma)$.

Despite the more rapid onset of masing brought by a spread of coupling strengths, the oscillation is weaker (power wise) and decays faster. This could be caused by the significance of frequency detuning between clusters with a wider spread coupling strength. These subtleties have yet to be explored and mapped out. With predicted advantages and disadvantages for

different distributions of coupling strengths, the maser can be quantitatively designed and optimized according to these trade-offs.

VII. CONCLUSIONS

In this study, we have implemented a more realistic quantum mechanical simulation of an optically pumped maser, where the magnetic field of the electromagnetic mode being amplified by stimulated emission varies in amplitude (and direction) over the volume of maser’s pumped gain material corresponding to a distribution of spin-photon coupling strengths. We also simulated our experiments using the mean-field approximation (MFA) along the lines of previous studies [4, 6], as a reference point.

Our experimental results revealed Rabi-like oscillations at the onset of the maser burst, with a frequency and duration that could be accurately reproduced by incorporating the experimental distribution of coupling strength into our simulation. This was done by expanding the Jaynes-Cummings model to encompass multiple “clusters” of spins, each with a different coupling strength. This distribution was faithfully modeled using a solver of Maxwell’s equations (namely COMSOL) based on the finite-element method. The remaining slight discrepancy in oscillation amplitude highlights the limitation of assuming a uniform optical pumping rate for all molecules, suggesting that spatial variation in the pumping should also be considered in any future, yet-more-accurate refinements. In contrast, our simulation invoking the MFA failed to capture the transient dynamics of the Rabi oscillations, with an overestimated coupling strength leading to a prolonged oscillation duration.

Beyond the initial oscillatory phase of the cavity’s photon number, we observed a steady maser output in both simulations, while the experimental output exhibited a gradual decline over time. This divergence can be attributed to thermal loading effects, as the temperature rise in the Pc:Ptp crystal enhances spin-lattice relaxation and detuning, consistent with previous studies.

By constructing artificial distributions of coupling strengths [these were Gaussian in form each possessing a different width (standard deviation) of σ], several trends were observed with increasing σ : (i) an

*contact author: xinpeng.shu23@imperial.ac.uk

† contact author: yining.jiang23@imperial.ac.uk

increased Rabi frequency; (ii) shortened initial delay for the onset of maser and (iii) a decreased pumping threshold caused by increasing standard deviation. Tied to completely defined, reproducible model, these trends provide insight into the maser's operation at the quantum mechanical level, allowing such devices to be engineered/optimized for specific purposes.

ACKNOWLEDGMENTS

M.O. acknowledges support from EPSRC's New Horizon's grant EP/V048430/1, "Tiger in Cage"

APPENDIX

-
- [1] D Burgarth, P Facchi, R Hillier, M Ligabò, Taming the rotating wave approximation, *Quantum* **8**, 1262, 2024.
- [2] W. E. Lamb Jr, "Theory of an optical maser," *Physical review*, vol. 134, no. 6A, p. A1429, 1964.
- [3] M. Oxborrow, J. D. Breeze, and N. M. Alford, "Room-temperature solid-state maser," *Nature*, vol. 488, no. 7411, pp. 353-356, 2012.
- [4] J. D. Breeze, E. Salvadori, J. Sathian, N. M. Alford, and C. W. Kay, "Room-temperature cavity quantum electrodynamics with strongly coupled Dicke states," *npj Quantum Information*, vol. 3, no. 1, p. 40, 2017.
- [5] E. Salvadori et al., "Nanosecond time-resolved characterization of a pentacene-based room-temperature MASER," *Scientific reports*, vol. 7, no. 1, p. 41836, 2017.
- [6] H. Wu et al., "Room-temperature quasi-continuous-wave pentacene maser pumped by an invasive Ce: YAG luminescent concentrator," *Physical Review Applied*, vol. 14, no. 6, p. 064017, 2020.
- [7] S. Bogatko et al., "Molecular design of a room-temperature maser," *The Journal of Physical Chemistry C*, vol. 120, no. 15, pp. 8251-8260, 2016.
- [8] J. Wrachtrup, C. von Borczyskowski, J. Bernard, M. Orrit and R. Brown, "Optically detected spin coherence of single molecules", *Phys. Rev. Lett.* **71**, pp. 3565-3568, 1993.
- [9] M Iinuma, Y Takahashi, I Shaké, M Oda, A Masaike, T Yabuzaki, and HM Shimizu, "High proton polarization at high temperature with single crystals of aromatic molecules", *Nuclear Instruments and Methods in Physics Research Section A: Accelerators, Spectrometers, Detectors and Associated Equipment* **529**, pp. 199-203, 2004.
- [10] D. J. Sloop, H. L. Yu, T. S. Lin, and S. Weissman, "Electron spin echoes of a photoexcited triplet: Pentacene in p-terphenyl crystals," *The Journal of Chemical Physics*, vol. 75, no. 8, pp. 3746-3757, 1981.
- [11] H. J. Carmichael, *Statistical methods in quantum optics 1: master equations and Fokker-Planck equations*. Springer Science & Business Media, 2013.
- [12] D. Plankensteiner, C. Hotter, and H. Ritsch, "QuantumCumulants. jl: A Julia framework for generalized mean-field equations in open quantum systems," *Quantum*, vol. 6, p. 617, 2022.
- [13] J. Breeze, E. Salvadori, J. Sathian, *et al.* Continuous-wave room-temperature diamond maser. *Nature* **555**, 493-496 (2018). <https://doi.org/10.1038/nature25970>
- [14] M. Ivill, E. Ngo, and M. W. Cole, "Method and characterization of pyroelectric coefficients for determining material figures of merit for infrared (IR) detectors," *Army Research Lab Aberdeen Proving Ground Md Weapons and Materials Research Directorate: Aberdeen, MD, USA*, 2013.
- [15] Q. Wu, Y. Zhang, X. Yang, S.-L. Su, C. Shan, and K. Mølmer, "A superradiant maser with nitrogen-vacancy center spins," *Science China Physics, Mechanics & Astronomy*, vol. 65, no. 1, p. 217311, 2022.
- [16] M. Blaha, A. Johnson, A. Rauschenbeutel, Arno and J. Volz, "Beyond the Tavis-Cummings model: Revisiting cavity QED with ensembles of quantum emitters", *Phys Rev A* **105**, 013719, 2022.
- [17] M. Goryachev, L. Zhao, Z. Zhao, W. G. Farr, J. Krupka, and M. E. Tobar, "Determination

*contact author: xinpeng.shu23@imperial.ac.uk

† contact author: yining.jiang23@imperial.ac.uk

- of the Anisotropy of Permittivity of Quantum Paraelectric Strontium Titanate",
- [19] Q. Wu et al., "Superradiant Masing with Solid-state Spins at Room Temperature," arXiv preprint arXiv:2212.01864, 2022.
 - [20] J.-L. Ong, D. J. Sloop, and T.-S. Lin, "Deuteration effect on the spin dynamics of the photo-excited triplet state of pentacene in p-terphenyl crystals," *Chemical physics letters*, vol. 241, no. 5-6, pp. 540-546, 1995. arXiv preprint arXiv:1508.07550, 2015
 - [18] J. Sathian, J. D. Breeze, B. Richards, N. M. Alford, and M. Oxborrow, "Solid-state source of intense yellow light based on a Ce: YAG luminescent concentrator," *Optics Express*, vol. 25, no. 12, pp. 13714-13727, 2017.
 - [21] P. Zappi, E. Farella, and L. Benini, "Tracking motion direction and distance with pyroelectric IR sensors," *IEEE Sensors Journal*, vol. 10, no. 9, pp. 1486-1494, 2010.
 - [22] M. Oxborrow, "Maser Assembly", US Patent 9608396B2, 2017 (granted).
 - [23] G. Khitrova et al, "Vacuum Rabi splitting in semiconductors," *Nature Physics*, vol. 2, (2), pp. 81–90, 2006.

*contact author: xinpeng.shu23@imperial.ac.uk

† contact author: yining.jiang23@imperial.ac.uk